# Nonstatistical fluctuations in the $^{35}$Cl$(n, p)^{35}$S reaction cross section at fast-neutron energies from 0.6 to 6 MeV

S. A. Kuvin [ORCID], H. Y. Lee [ORCID], T. Kawano, B. DiGiovine [ORCID], A. Georgiadou [ORCID], C. Vermeulen, M. White, and L. Zavorka [ORCID]

*Los Alamos National Laboratory, Los Alamos, New Mexico 87545, USA*

H. I. Kim

*Nuclear Physics Application Research Division, Korea Atomic Energy Research Institute, Yuseong-gu, Daejeon, Korea*

The lack of experimental data on the $^{35}$Cl$(n, p)^{35}$S reaction above 100 keV has led to nuclear data evaluations that are relatively unconstrained at fast neutron energies. As a result, efforts to explore, develop, and potentially certify next generation reactor designs that incorporate chloride salts as a coolant material have been hindered. In this paper, we report partial cross section data for the $^{35}$Cl$(n, p)^{35}$S and $^{35}$Cl$(n, \alpha)^{32}$P reactions at incident neutron energies between 0.6 MeV and 6 MeV. The measurement was performed using the pulsed beam of neutrons at the unmoderated WNR spallation neutron source at the Los Alamos Neutron Science Center, with the outgoing charged particles detected by the LENZ experimental setup, consisting of annular silicon detectors. Nonstatistical fluctuations in the $^{35}$Cl$(n, p_0)$ cross section were observed up to around 3 MeV, and the magnitude of the cross section was systematically lower than all available data evaluations at energies above 1 MeV. Modifications to the ENDF/B-VIII.0 data evaluation are suggested to better reproduce the energy averaged experimental data.

## I. INTRODUCTION

Advanced nuclear-reactor designs explore various coolant materials beyond regular water cooling, such as chloride salt in molten salt reactors (MSRs). Such efforts are relatively recent and, as a result, the nuclear reaction data on some of the relevant elements are not available or are lacking in precision. The lack of experimental data on the $^{35}$Cl$(n, p)^{35}$S reaction at neutron energies from 100 keV to 14 MeV, has led to a large variation among different nuclear data evaluations [1–3], as shown in Fig. 1.

The low level densities for nuclei in this mass-range indicate that a more microscopic treatment to the calculations may be necessary, hindering the applicability of a statistical Hauser-Feshbach [4] approach to the entire energy range. To this end, a resolved resonance approach [5] was employed in the transition from ENDF/B-VII.0 to ENDF/B-VII.1 for the $^{35}$Cl$(n, p)$ cross section, up to approximately 1.2 MeV, based on total cross section measurements performed on $^{nat}$Cl [6] and direct measurements of $^{35}$Cl$(n, p)$ up to 100 keV [7,8]. Above 1.2 MeV, there is a transition to an energy-averaged approach that ties in to the available experimental data at 14 MeV [9–11].

A recent study by Batchelder *et al.* [12], provides evidence that a non-statistical, resolved resonance approach to evaluating the $^{35}$Cl(n,p) cross section may be necessary up to nearly 3 MeV, which is inconsistent with all available evaluations. In the context of fast spectrum MSRs, the results are enticing because a reduction in the cross section at peak neutron energies between 1–3 MeV would imply that less $^{35}$S, a long-lived radioisotope with a half-life of 87.5 d, would

be produced in systems that incorporate unenriched chloride salts. That is, the path to certification for such designs would be less sensitive to enrichment and potentially be more cost-effective.

Further evidence for possible nonstatistical behavior in the $^{35}$Cl$(n, p)$ cross section comes from a study characterizing the detector response of $^6$Li-depleted CLYC (C7LYC) detectors [13], for which the dominant detection mechanism for fast
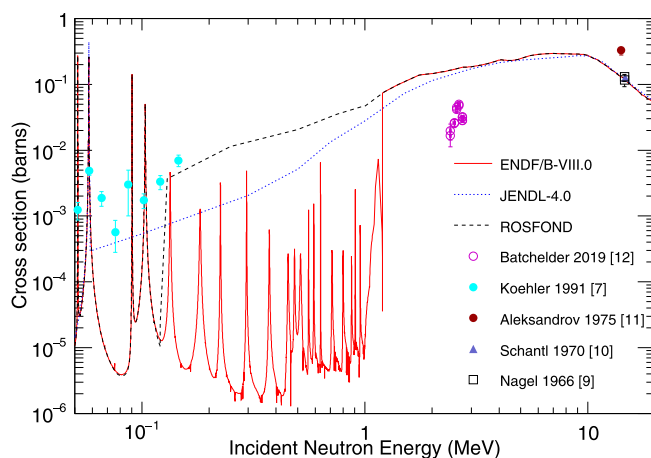


FIG. 1. The $^{35}$Cl$(n, p)^{35}$S reaction cross section, highlighting the lack of experimental data between 100 keV and 14 MeV. Recent data from Ref. [12] show a dramatic reduction in the cross section relative to all available evaluations and suggests that a resolved resonance approach may be necessary as high as 3 MeV.

TABLE I. Summary of the multiple subsets of data taken with the NaCl sample. The uncertainty represented in the distance between target sample and the WNR neutron source for the 15 degree flight path is given by half the length of the tungsten target. The uncertainty for the 90 degree flight path is given by the radius of the target.

| Setup | WNR flight path | Sample thickness | Distance T4 to sample (m) | Integrated neutron fluence at $E_n = 3$ MeV | Detector distance from sample (mm) | | | |
|---|---|---|---|---|---|---|---|---|
| | | | | | A | B | C | D |
| 1 | 90L | $350 \,\mu g/cm^2$ | 8.093(15) | $1.03 \times 10^{11}$ n/MeV | −76.9 | −71.9 | −35.9 | N/A |
| 2 | 15R | $450 \,\mu g/cm^2$ | 15.200(37) | $6.80 \times 10^{11}$ n/MeV | +20 | +41 | +91 | N/A |
| 3 | 15R | $350 \,\mu g/cm^2$ | 14.191(37) | $5.04 \times 10^{11}$ n/MeV | −109 | −101 | −42 | −34 |

neutrons is via $^{35}$Cl$(n, p)$. Unexpected resonance-like structures were observed in the neutron time-of-flight spectrum for incident neutrons above 1 MeV [14]. Therefore, a precise measurement of the $^{35}$Cl$(n, p)$ cross section is crucial for proper characterization of the efficiency for CLYC and C7LYC detectors at fast neutron energies. It follows that measurements of C7LYC detector efficiency [15–17] can be used to further validate measurements of the $^{35}$Cl$(n, p)$ cross section.

## II. EXPERIMENT

### A. Unmoderated neutron source at LANSCE

The experiment was performed at the WNR facility at the Los Alamos Neutron Science Center (LANSCE) [18]. The LANSCE accelerator delivers 800 MeV protons to the unmoderated tungsten target at WNR, generating neutrons with a broad energy spectrum via spallation. The target is cylindrical in shape with dimensions of 7.5 cm in length and 3 cm in diameter. The proton beam impinges on its front base and the outgoing neutrons are collimated and delivered to multiple experimental stations. In this work, measurements were taken at flight path 90L, which is oriented at a 90 degree angle with respect to the proton beam, and at flight path 15R, which is oriented at a 15 degree angle.

The time structure of the proton beam consisted of either 20 or 40 macropulses/s, with each 625 $\mu$s long macropulse consisting of approximately 340 micropulses, each separated by 1.8 $\mu$s. Depending on the flight path length, the time structure imposes a minimum neutron energy before frame overlap occurs, and the low energy neutrons can no longer be distinguished from the high energy neutrons of the subsequent pulse. For example, at a flight path length of 15 m, the minimum energy that can be resolved is approximately 300 keV.

### B. Experimental setup

The outgoing charged particles from $(n, p)$ and $(n, \alpha)$ reactions were detected using the low energy $(n, z)$ (LENZ) experimental setup [19], consisting of annular double-sided silicon strip detectors, at both the 15R and 90L flight paths of WNR. The targets consisted of 450 $\mu$g/cm$^2$ and 350 $\mu$g/cm$^2$ NaCl samples ($^{35}$Cl enriched to 99.35%) that were each evaporated on to a 4.88 mg/cm$^2$ brass backing, consisting of 65% Cu and 35% Zn. The neutron flux was actively monitored via $^{238}$U$(n, f)$ with an ionization detector loaded with a $^{238}$U foil [20]. A summary of the different experimental configurations is summarized in Table I and a sketch of the general LENZ setup is shown in Fig. 2. A conservative estimate of 10% for

the uncertainty in the NaCl sample thickness has been adopted and listed in Table II.

For each flight path, the location of the experimental setup and the end of the beam collimation, relative to the WNR target, was measured using a combination of LIDAR and optical CMM laser scanning techniques. A precise measurement of the flight path length was made using a sCVD diamond detector [21], by measuring the neutron time of flight associated with the 2.078 MeV neutron scattering resonance in $^{12}$C (a standard for neutron time-of-flight measurements). Consistency checks were also made by measuring the neutron time of flight for the low energy resonances in the $^{238}$U$(n, f)$ spectrum from the ionization chamber and the resonances in $^{14}$N$(n, p)$ $^{14}$C observed with a kapton target. From each of the different methods, the reaction target position relative to the WNR neutron source was reproduced consistently to within 5 mm and within 1 cm of the expected location as determined by the LIDAR measurements. The optical CMM laser scanning techniques that we employ allow us to take sub-mm resolution scans of the experimental setup, however, the resolution for measuring the distance to the WNR target was on the order of 1 cm due to the inherent accuracy of the LIDAR system and due to limited return data available when imaging the target directly down the flight path penetrations. The uncertainties for the flight path length between the neutron source and the target sample in Table I are given as half the length of the tungsten target for 15R (37 mm) and half the radius (15 mm) for 90L.
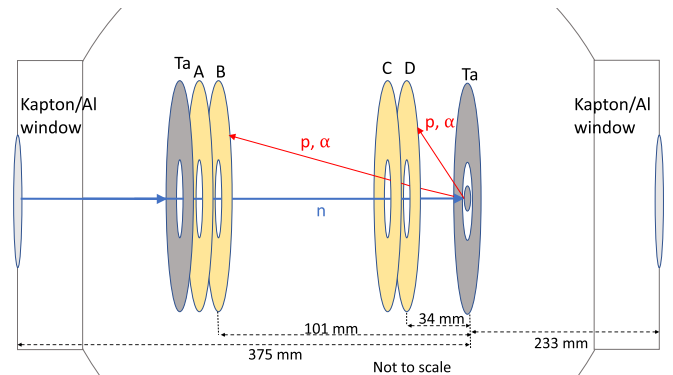


FIG. 2. Sketch of experimental setup 3, as described in Table I, consisting of annular silicon detectors and a NaCl target. The direction of the beam defines the $+z$ axis. The target is supported by a tantalum sheet with the same dimensions as an S1-type silicon detector.

TABLE II. Summary of the sources of systematic uncertainty analyzed in this work. The neutron energy uncertainty incorporates the intrinsic timing resolution of the silicon detectors, the uncertainty in the recoil correction, and the finite length of the WNR target as described in Table I. The uncertainty ranges for the background shape are for the $(n, p_0)$ and $(n, p_{x>0})$ reaction channels, respectively.

| Systematic uncertainty source | Value |
| --- | --- |
| TOF uncertainty (detector res. FWHM) | 4–5 ns |
| TOF uncertainty (recoil TOF correction) | $\leqslant 0.5$ ns |
| Neutron energy uncertainty ($L = 14$ m,15 m) | 2–60 keV |
| Neutron energy uncertainty ($L = 8$ m) | 3–100 keV |
| Flux normalization | 8–9 % |
| Sample thickness | <10 % |
| Background shape | 5–15 %, 5–50 % |
| Deadtime | $\leqslant 1\%$ |
| Solid angle/detector efficiency | 1–4 % |

At the 15R flight path, the neutron beam was collimated to a 0.7 inch diameter and the NaCl target was located at distances of either 15.200(37) m (setup 2) or 14.191(37) m (setup 3) relative to the spallation target, as described in Table I. At the 90L flight path, the neutron beam was collimated down to a quarter-inch diameter and the NaCl target was placed at a distance of 8.093(15) m. Three annular double-sided silicon strip detectors (DSSDs) were used in this setup, at locations of $-36$ mm, $-72$ mm, and $-77$ mm relative to the NaCl target, as shown in Fig. 2. The detectors at $-72$ mm and $-77$ mm were S3-type detectors [22] with thicknesses of 300 $\mu$m and 1500 $\mu$m, respectively. These detectors form a $\Delta E$-$E$ telescope configuration and, in addition to allowing for particle identification, enable the rejection of charged particle events that do not originate from the target position. The detector at $-36$ mm, and all of the detectors used on 15R, were S1-type detectors with a larger inner diameter (48 mm) than the S3 detectors. For setup 2, the thicknesses for detectors labeled A, B, and C were 65 $\mu$m, 300 $\mu$m, and 500 $\mu$m, respectively. For setup 3, the thicknesses were 500 $\mu$m, 300 $\mu$m, 1000 $\mu$m, and 500 $\mu$m, respectively. The angular range subtended by each detector ring and the solid angle coverage is determined from an MCNP simulation [23] of the experimental setup. In this current configuration, the setups are optimized for total efficiency with solid angle coverages between 1.0 and 1.6 sr for each setup.

In most cases, the upstream most silicon detector was used to identify and veto events that originate from neutron induced charged particle reactions on the vacuum window, consisting of foils of 0.075 mm of Kapton and 0.024 mm of aluminium, and light charged particles that come with the neutron beam and originate from the spallation target or from secondary reactions due to the neutron beam collimation. To further cut down on the background due to low energy charged particles, 150 $\mu$m tantalum sheets with identical planar geometry as the silicon detectors were placed between the vacuum chamber windows and the upstream and downstream most silicon detectors. For the configuration where all of the detectors are downstream of the target, and no detector can serve as a veto,

we rely solely on background subtraction from blank target data taken without a NaCl sample.

### C. Data acquisition

Signals from the LENZ detectors and fission flux monitors were readout using a digital data acquisition system consisting of 16-channel CAEN VX1730 digitizers. The digitizers were programed with CAEN DPP-PSD firmware and all trigger events from each channel were accepted, with each individual trigger determined by a leading edge discriminator. For each triggered event, a waveform consisting of 800 samples (1600 ns) was recorded. The independent triggering, coupled to the 1.8 $\mu$s beam time structure ensures a nearly negligible data acquisition deadtime.

To improve the timing response for each channel, and correct for walk, a constant fraction or double derivative filter was applied offline to the waveforms. The filter parameters were optimized on a channel by channel basis to achieve the best relative timing resolution between each side of the DSSDs and relative to the "T0" signal that comes from the proton pickoff detector just before the WNR tungsten target. Each detector channel is aligned relative to the well-defined, prompt timing signal that originates from the arrival of $\gamma$ rays from the spallation target. An additional timing correction is performed on a run-by-run basis to correct for any time-shifts that may occur during the digitizer synchronization at the start of each run. The resulting FWHM of the prompt $\gamma$-flash peak is typically between 4 and 5 ns and this defines the timing resolution of the LENZ detectors in this work. The resulting energy uncertainty is given in Table II, for each setup/flight path length.

Validation of the signals from a single detector is performed offline by requiring a time coincidence window of 15 ns between signals from both sides of the DSSDs and a matching energy requirement. An energy add-back algorithm is used to sum events where energy may be split between adjacent rings of the detector. In addition, only signals that come within a 15 $\mu$s window of the most recent "T0" signal are accepted. Finally, runs where the beam was operating in off-normal conditions are rejected and are typically identified by low yields in the flux monitor.

## III. ANALYSIS

### A. Beam normalization

The shape of the neutron flux was characterized for both the 15R and 90L flight paths using ionization chambers loaded with $^{238}$U and $^{235}$U foils. The $^{238}$U$(n, f)$ reaction was used to characterize the flux for neutron energies above 2 MeV and the $^{235}$U$(n, f)$ reaction used for neutron energies below 2 MeV. As described in Refs. [20,24], the contribution due to wrap-around neutrons in the $^{235}$U fission yield is corrected for by measuring the events that come after the final micropulse from each macropulse. Typical uncertainties in the wraparound correction are between 1–4 % for the range of neutron energies up to 1.8 $\mu$s and this is included in the beam normalization uncertainty in Table II. The ion chamber with the $^{238}$U foil was used to actively monitor the neutron

flux throughout all of the experiments and, due to the fission threshold at approximately 1.5 MeV, was used to monitor the quality of the beam tune by identifying off-time events that are associated with LANSCE proton dark current. This dark current refers to the protons arriving to the spallation target in between the expected micropulse/macropulse time structure of the proton beam bunching. These protons do not form a high enough current to trigger the "T0" proton pick off signal and therefore contribute as a continuous background of events relative to the most recent bunched micropulse. Further discussion on the nature of the proton dark current can be found in Ref. [18]. The total dark current contribution for the accepted runs in this work was typically between 0.001% and 0.01%.

### B. Source calibrations

An $\alpha$-emitting source of $^{229}$Th and a mixed isotope source consisting of Am, Cm, and Pu radioisotopes were used to calibrate the energy scale and linearity of the detectors. The sources were placed at the target position and an energy correction was applied to account for the different energy loss for incident protons through the detector dead-layer, using energy loss tables from SRIM [25]. In addition to the window of the DSSDs, an additional Si-dead-layer uncertainty of $0.5\,\mu$m was included to account for detector damage and nonuniformities. This uncertainty propagates into the recoil time of flight correction uncertainty that is discussed in Sec. III C. The known activity of the mixed isotope source was also used to verify the solid angle coverage of each detector, as determined by the MCNP simulation. The uncertainty in the solid angle coverage is determined by varying the relative distance, along the beam axis, between the detectors and the target by 1 mm.

### C. Reconstruction of the reaction $Q$ value

The reaction $Q$ value is reconstructed from the detected energy and angle of the outgoing charged particle and from the incident neutron energy that is determined by the time of flight from the spallation target to the silicon detectors. A recoil time of flight correction is applied to account for the finite time of flight of the detected charged particle from the target to the detectors so the incident neutron energy is given by

$$T_n = T_{\text{det}} - T_0 - T_{\text{recoil}} + L/c, \qquad (1)$$

where $T_n$ is the incident neutron time of flight, $T_{\text{det}} - T_0$ is the offline corrected timestamp of the silicon detector event relative to the proton pick-off signal (after aligning the detectors so that the prompt $\gamma$ peak is centered at zero), $T_{\text{recoil}}$ is the nonrelativistic recoil time of flight correction, and $L/c$ is the time of flight for a $\gamma$ ray to travel the length of the flight path ($L$). The correction is different for each detector and is determined by the detector distance and the detected charged particle energy, with corrections applied based on whether the detected particle is expected to be an alpha or a proton. The uncertainty due to the recoil time of flight correction is typically $\leqslant 1$ ns and is reflected in Table II. The correlation between the detected charged particle energy and the neutron time of flight (with respect to the arrival of the $\gamma$ rays) for a single detector is shown in Fig. 3. Different
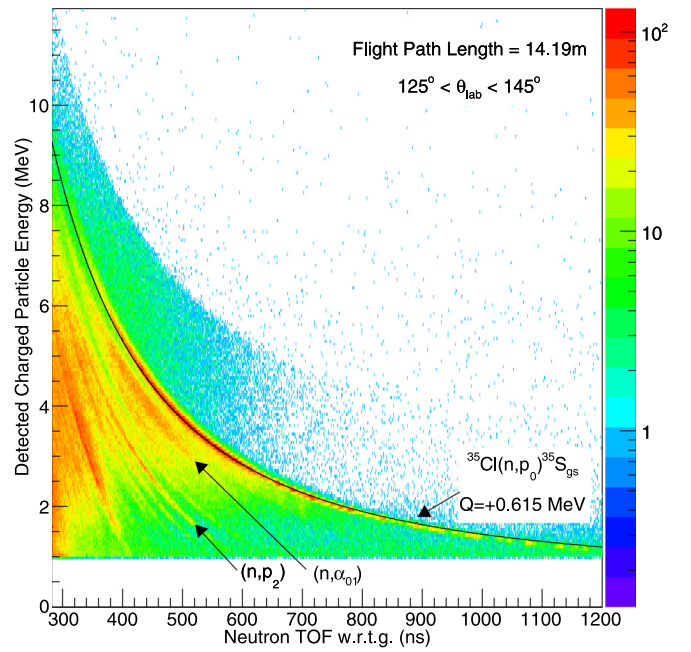


FIG. 3. The detected charged particle energy of the outgoing proton or $\alpha$ particle, and the corresponding neutron time-of-flight, is used to reconstruct the $Q$ value of the reaction channel.

reaction channels are identified by the kinematic curves which correspond to a particular reaction $q$ value. $^{35}$Cl$(n, p)$ reaction channels populating up to the fifth excited state in $^{35}$S are cleanly observed above the background contributions that are discussed in Sec. III D.

As a consequence of the timing structure of the proton beam at LANSCE, the delayed neutron events with a sufficiently low energy, depending on the flight path distance, will wrap around and be indistinguishable from the higher energy neutrons of the following pulse. As a result, there is a hard cut off in the lowest neutron energy detected, just before the $\gamma$ flash of the following pulse. In the case of the $^{35}$Cl$(n, p)^{35}$S reaction, which does not have a threshold, low energy neutron events that wrap-around will be misidentified as having a higher neutron energy and thus the reconstructed reaction $Q$ value will not match to the expected value. In addition, a software cut is placed at detected particle energies above 1 MeV to cut out the low energy beam-induced backgrounds. This results in a low neutron energy limit of around $\approx 500$ keV for detecting $^{35}$Cl$(n, p)$ events.

### D. Background analysis

The primary sources of background in the work are due to $(n, z)$ reactions on the vacuum window at the entrance to the experimental chamber, on the brass backing material in the target, and due to incident light charged particles that come with the neutron beam and originate from the spallation target and/or collimation. For the latter, the incident charged particles are typically of very high energy (greater than 100 MeV) and deposit only small amounts of energy in the detectors with a prompt time of flight. As previously mentioned, these events, along with the charged particles that originate
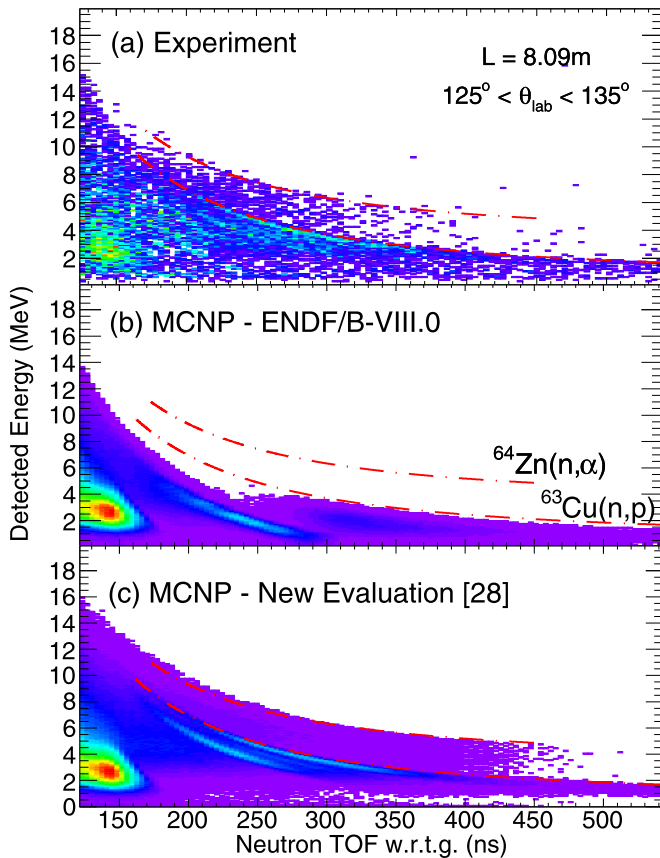
FIG. 4. (a) Experimental data for all $(n, z)$ reactions on a brass target (65% Cu, 35% Zn) as compared to (b) an MCNP simulation using the unmodified ENDF/B-VIII.0 as an input and (c) an MCNP simulation using the newly evaluated energy spectra [28], based on ENDF/B-VIII.0 cross sections, as an input. In the unmodified ENDF/B-VIII.0, there is no outgoing charged particle spectrum for the $\alpha$ particles from $^{64}Zn(n, \alpha)$.



FIG. 5. (a) Comparison between brass backing data and the modified MCNP simulation and, for the same energy range, (b) the NaCl data with fit $(n, p)$ and $(n, \alpha)$ signals for the first few excited states of $^{35}S$ and $^{32}P$. The components of the simulated spectrum are shown in (a) for $(n, p)$ reactions on brass (orange dashed line) and $(n, \alpha)$ reactions on brass (magenta thin solid line).

from the vacuum window, are identified in the upstream-most detector and most of these events can be vetoed. The remainder of the neutron beam induced background is characterized through analysis of runs without a target sample. Background lines due to $^{28}Si(n, p)^{28}Al$ and $^{28}Si(n, \alpha)^{25}Mg$ are observed at energies above $E_n = 5$ MeV, however, these lines only begin to interfere with the extraction of $^{35}S$ excited states above 3 MeV in excitation energy [above the $(n, p_5)$ reaction channel]. In the forward angle data, an additional source of background is attributed to $^1H(n, p)n$ reactions due to target contamination. However, due to the rapid variation of outgoing proton energy with respect to the emission angle, these events do not interfere with the extraction of the $^{35}Cl(n, p_0)$ and $^{35}Cl(n, \alpha_{01})$ reaction yields although they do result in a worse signal to background ratio for extracting the higher excited state yields. Finally, data was recorded with the brass backing material alone to characterize the background from $(n, z)$ reactions on Cu and Zn.

The experimental data with the brass target, along with Fe and Ni targets, were used to validate MCNP [23] and GEANT4 [26] simulations of the LENZ experimental setup, as shown in Fig. 4. As part of this effort, we demonstrated
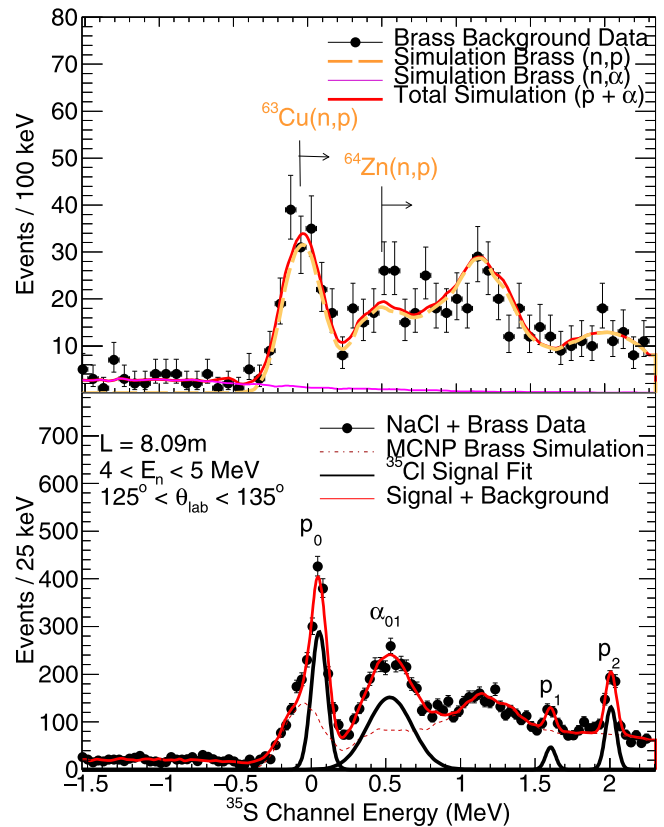
the need for improved evaluations of the $(n, p)$ and $(n, \alpha)$ reactions on certain stable nuclei, which are used as inputs for MCNP and GEANT4 [27], to accurately predict the experimental backgrounds. Specifically, the need for additional double differential cross section information that incorporate the discrete population of excited states. For this application, the current ENDF/B-VIII.0 evaluation included no outgoing particle spectrum for the $^{64}Zn(n, \alpha)$ reaction and, as a result, the $\alpha$ particles observed in the LENZ brass data could not be reproduced in the simulation. In addition, the general shape of the proton spectrum could not be reproduced until modifying the evaluation for the $^{63}Cu(n, p)$ and $^{64}Zn(n, p)$ reactions. New evaluations on the outgoing particle spectrum, based on unchanged ENDF/B-VIII.0 reaction cross sections, of $(n, z)$ reactions for 62 isotopes were performed by Kim *et al.* [28] and are included in our MCNP simulation.

With the implementation of the new evaluation, the experimental data on the brass foil is reproduced very well by the simulation, as shown in Fig. 5(a). The simulated shape of the background is then used to fit the background component of the experimental data with the NaCl target to extract partial differential cross sections for the $^{35}Cl(n, p)$ and $^{35}Cl(n, \alpha)$ reactions, as shown in Fig. 5(b) for incident neutron energies between 4 to 5 MeV. Contributions due to $^{23}Na(n, p)^{23}Ne$ and
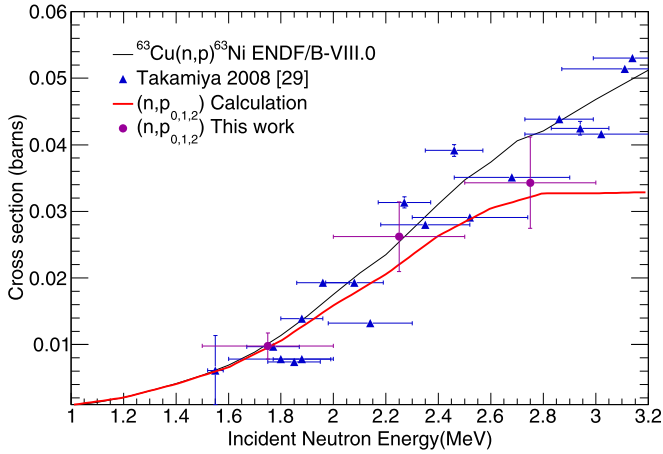
FIG. 6. The $^{63}$Cu$(n, p_{0,1,2})$ $^{63}$Ni contribution to the brass backing data shows good agreement with the ENDF/B-VIII.0 cross section evaluation and previous measurements [29] and is used as a consistency check for the beam normalization in this work. The calculation of the partial cross section contribution to the total cross section was calculated using the Hauser-Feshbach code COH3 [30].

$^{23}$Na$(n, \alpha)$ $^{20}$F, which have larger negative $Q$ values, do not interfere in the extraction of the first few excited states of $^{35}$S and $^{32}$P.

Furthermore, the data on the brass backing material allowed us to perform a consistency check for the beam normalization. As shown in Fig. 5(a), the broad peak at approximately zero excitation energy corresponds to the $^{63}$Cu$(n, p)$ reaction to the ground state ($Q = 0.63$ MeV) and the first few excited states of $^{63}$Ni. The contributions to the events at higher excitation energies include the reactions leading to higher excited states of $^{63}$Ni, as well as the other dominant reaction channels from natural copper and zinc [e.g., $^{64}$Zn$(n, p)$ and $^{65}$Cu$(n, p)$]. However, at energies up to 3 MeV, the total cross section for $^{63}$Cu$(n, p)$ is determined primarily by the $^{63}$Cu$(n, p_{0,1,2})$ reaction channels, as shown in Fig. 6. The energy-angle-integrated cross sections based on the yields from the $^{63}$Cu$(n, p_{0,1,2})$ reactions studied here are also shown in Fig. 6 and are in good agreement with the ENDF/B-VIII.0 cross section evaluation.

The uncertainty due to the background shape, listed in Table II, was between 5–15 % for extracting the $p_0$ partial cross section and as high as 50% for extracting the higher excited states. Therefore, the total systematic uncertainties were between 15–20 % for the ground state and between 15–50 % for the higher excited states. Unless otherwise noted, the error bars on all plots in this work include both systematic and statistical uncertainties.

Planned future studies will improve the systematics by performing the measurement with enriched $^{35}$Cl of different forms, such as NaCl and AgCl, and with isotopically pure Au or Pt backing materials instead of brass. An improved choice in the backing material will allow us to extend our measurement to higher incident neutron energies, while also dramatically reducing the background at the low energies currently under study.
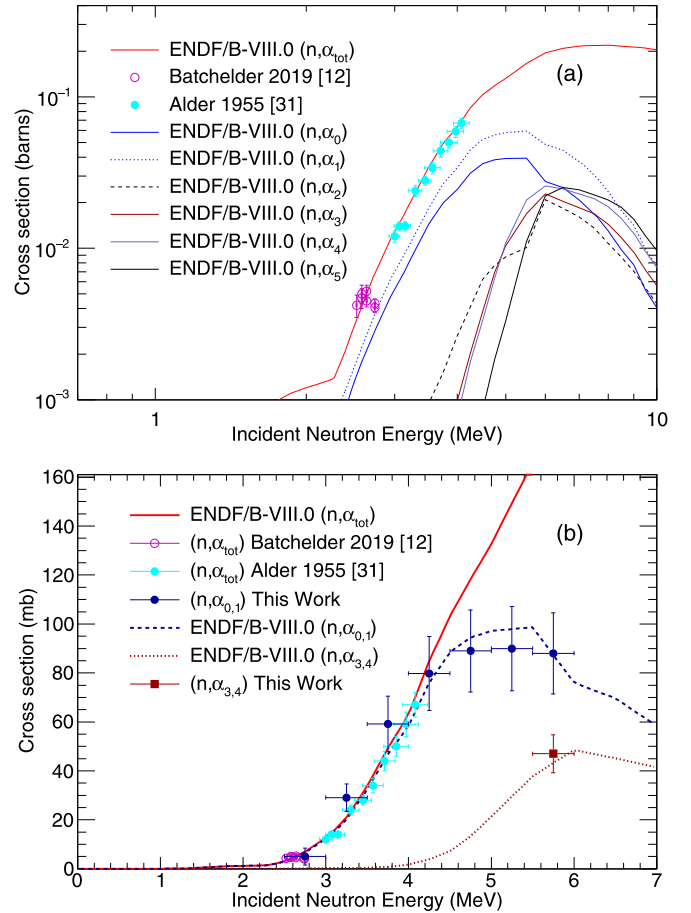


FIG. 7. Top: A comparison of past experimental data with the current ENDF/B-VIII.0 evaluation. The ENDF/B-VIII.0 library also includes partial cross sections for populating different excited states of $^{32}$P. Bottom: Experimental data from this work, summing the yield for the $(n, \alpha_0)$ and $(n, \alpha_1)$ reaction channels, is in good agreement with the current ENDF/B-VIII.0 library.

### E. Study of $^{35}$Cl$(n, \alpha)$ $^{32}$P

In the energy range above 1 MeV, the $^{35}$Cl$(n, \alpha)$ $^{32}$P reaction has been studied in various past measurements [9,12,31] and the ENDF/B-VIII.0 evaluation reproduces the past experimental data well, as shown in Fig. 7. Up to approximately 5 MeV, the $(n, \alpha)$ cross section is expected to be dominated by the sum of the $(n, \alpha_0)$ and $(n, \alpha_1)$ reactions that increase at approximately the same rate with respect to increasing neutron energy. Since the two final states in $^{32}$P are separated by only 78 keV [32], we observe both the $(n, \alpha_0)$ and $(n, \alpha_1)$ reaction channels as a single broad peak centered around their mean energy, as shown in Fig. 5(b).

Although the reaction $Q$ value for $(n, \alpha)$ is higher than $(n, p)$ by about 300 keV, the kinematics for the $(n, \alpha)$ reaction varies more rapidly than $(n, p)$ with increasing angle and due to different energy losses in the target and dead layer of the silicon detector, the $(n, \alpha_{0,1})$ peak is cleanly separated from the $p_0$ reaction channel at backward angles. At forward angles, there is very little separation between $(n, p_0)$ and $(n, \alpha_{0,1})$ as shown in Fig. 8, however the $(p_0)$ contribution
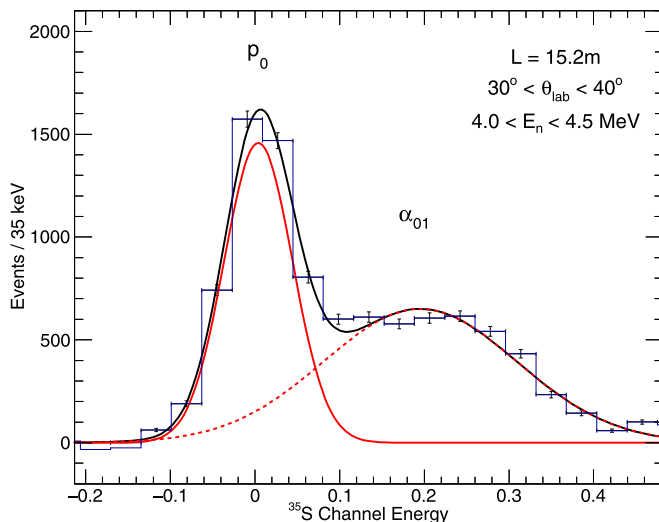
FIG. 8. Background subtracted excitation energy spectrum at forward angles. The $(n, p_0)$ reaction channel is identified by its narrow profile at the expected energy.

is identified by its narrow profile at the expected energy. In most cases, contributions due to the $(n, \alpha)$ reaction leading to higher excited states in $^{32}P$ could not be discriminated from the background shape discussed in the previous section. However, the 65 $\mu$m silicon detector in setup 2 could be used to cleanly identify contributions due to $(n, \alpha)$ at $E_n > 3$ MeV, as protons with energies above 3.5 MeV will pass through the detector before losing their full energy.

Measured partial differential cross sections for $(n, \alpha_0 + \alpha_1)$, from 5 to 6 MeV, are shown in Fig. 9. The measured angular distributions are consistent with the calculations from Ref. [28], employing a Blatt-Biedenharn formalism [33] for calculating the angular distributions explicitly. For $(n, \alpha)$ the
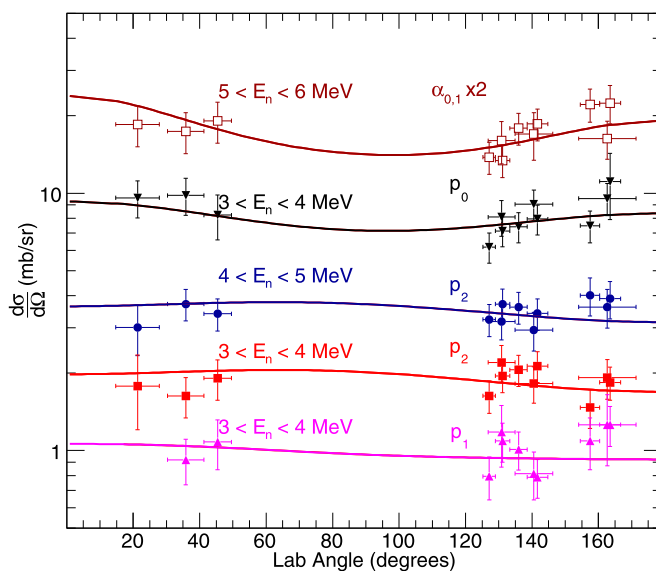


FIG. 9. Angular distributions for different reaction channels at various energies compared with calculations from Ref. [28]. The $\alpha$ channel is scaled by a factor of two for clarity.

angle-integrated cross sections are approximately 20% lower than if they were calculated assuming an isotropic distribution scaled by the weighted average of the experimental data points. The $(n, p)$ angular distributions show the similar feature of being symmetric about 90 degrees in the c.m. frame, however, the variation is not as dramatic. For this case, the cross sections are consistent to within 10%.

The energy- and angle-integrated partial cross sections, in 500 keV neutron energy bins, are given in Table III and shown in Fig. 7(b). The data point for the sum of the $(n, \alpha_{34})$ reaction channels is based on the yield from the 65 $\mu$m detector. The results are in good agreement with the current ENDF/B-VIII.0 evaluation.

## F. Study of $^{35}Cl(n, p)\,^{35}S$

Partial differential cross sections for the population of different excited states of $^{35}S$ via $^{35}Cl(n, p)$ are obtained by fitting the experimental data with Gaussian profiles at the known excitation energies of $^{35}S$ [34], as shown in Figs. 5(b) and 10. Similar to the case of $^{35}Cl(n, \alpha)$, the shape of the angular distribution is consistent with the calculations from Ref. [28] when the data are binned at 1 MeV incident neutron energy intervals, as shown in Fig. 9. The energy and angle integrated $(n, p)$ partial cross sections, in 500 keV incident energy intervals, are shown in Fig. 11 along with a comparison to the current ENDF/B-VIII.0 cross-section evaluation. Consistent with the conclusion presented by Batchelder *et al.* [12], the current ENDF/B-VIII.0 evaluation appears to be overestimating the $(n, p)$ cross section, but not as severely as previously suggested.

As already mentioned, the efficiency of CLYC detectors at fast neutron energies is sensitive to the $^{35}Cl(n, p)$ cross section. Thus, measurements of CLYC detector efficiency can be used to validate simulations that take differential cross sections as an input. Calculations of intrinsic CLYC detector efficiencies have been performed using simulation packages such as MCNP [16], however, it has been shown that proper modeling of the neutron transport and down scatter is also critical to accurately reproduce the detector response [16,17]. A study of CLYC detector efficiency at energies between 4.1 and 5.5 MeV was performed by Smith *et al.* [15] and from this efficiency they inferred a cross section for the $(n, p_0)$ reaction that is in good agreement with the results presented here, as shown in Fig. 11. This reduction in cross section for the $(n, p_0)$ reaction channel may also help explain the discrepancy in the pulse high spectra observed in Ref. [16] when compared with MCNP simulations incorporating the ENDF/B-VII.1 library.

No attempt is made to increase the number of energy bins for the experimental data leading to the excited states of $^{35}S$ to ensure an adequate ratio between the signal and background statistics. On the other hand, at incident neutron energies up to approximately 3 MeV, the yield for the $(n, p_0)$ reaction channel were adequate enough to bin the data into 2.5 ns wide time-of-flight bins (which approximately reflects the $\sigma$ of the silicon detector timing resolution). The background subtracted yield is then normalized by the integrated neutron flux over each energy bin to give the partial differential cross

TABLE III. Angle-integrated partial cross section data for $^{35}Cl(n, p)^{35}S$ and $^{35}Cl(n, \alpha)^{32}P$ at incident neutron energy intervals of 500 keV.

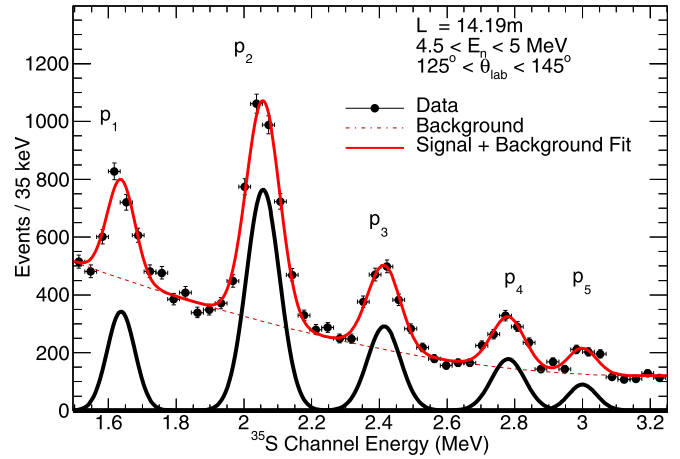| $E_n$ (MeV) | Reaction channel | $\sigma_{exp} \pm^{stat}_{sys}$ (mb) | $\sigma_{ENDF}$ (mb) |
|---|---|---|---|
| 1.25(25) | $(n, p_0)$ | $50.7 \pm^{5.0}_{8.2}$ | 80.0 |
| 1.75(25) | $(n, p_0)$ | $72.2 \pm^{1.5}_{11}$ | 137.8 |
| 2.25(25) | $(n, p_0)$ | $66.4 \pm^{2.9}_{10}$ | 154.3 |
| 2.75(25) | $(n, p_0)$ | $82.2 \pm^{2.4}_{12.3}$ | 173.0 |
| 2.75(25) | $(n, p_1)$ | $3.9 \pm^{1.25}_{1.5}$ | 5.9 |
| 2.75(25) | $(n, p_2)$ | $5.2 \pm^{1.9}_{1.5}$ | 3.4 |
| 3.25(25) | $(n, p_0)$ | $97.7 \pm^{3.1}_{14.7}$ | 159.4 |
| 3.25(25) | $(n, p_1)$ | $8.6 \pm^{2.4}_{1.7}$ | 15.0 |
| 3.25(25) | $(n, p_2)$ | $18.7 \pm^{1.7}_{2.8}$ | 16.7 |
| 3.25(25) | $(n, p_3)$ | $1.64 \pm^{0.8}_{0.6}$ | 2.33 |
| 3.75(25) | $(n, p_0)$ | $82.2 \pm^{6.1}_{12.4}$ | 143.1 |
| 3.75(25) | $(n, p_1)$ | $11.3 \pm^{1.8}_{2.3}$ | 22.7 |
| 3.75(25) | $(n, p_2)$ | $28.5 \pm^{2.6}_{4.5}$ | 36.5 |
| 3.75(25) | $(n, p_3)$ | $10.7 \pm^{1.8}_{1.9}$ | 10.76 |
| 3.75(25) | $(n, p_4)$ | $2.4 \pm^{1.3}_{1.0}$ | 3.7 |
| 3.75(25) | $(n, p_5)$ | $1.0 \pm^{0.6}_{0.4}$ | 1.0 |
| 4.25(25) | $(n, p_0)$ | $72.4 \pm^{5.5}_{11}$ | 120.2 |
| 4.25(25) | $(n, p_1)$ | $12.9 \pm^{2.0}_{2.5}$ | 24.4 |
| 4.25(25) | $(n, p_2)$ | $42.9 \pm^{3.5}_{6.8}$ | 48.3 |
| 4.25(25) | $(n, p_3)$ | $15.2 \pm^{2.6}_{2.7}$ | 21.3 |
| 4.25(25) | $(n, p_4)$ | $9.4 \pm^{2.4}_{1.8}$ | 12.1 |
| 4.25(25) | $(n, p_5)$ | $3.9 \pm^{1.7}_{1.2}$ | 5.0 |
| 4.75(25) | $(n, p_0)$ | $66.3 \pm^{5.4}_{9.5}$ | 93.4 |
| 4.75(25) | $(n, p_1)$ | $8.7 \pm^{2.0}_{1.8}$ | 23.2 |
| 4.75(25) | $(n, p_2)$ | $40.8 \pm^{4.0}_{6.5}$ | 48.5 |
| 4.75(25) | $(n, p_3)$ | $18.6 \pm^{3.1}_{3.3}$ | 25.2 |
| 4.75(25) | $(n, p_4)$ | $15.1 \pm^{3.0}_{3.0}$ | 19.8 |
| 4.75(25) | $(n, p_5)$ | $9.8 \pm^{2.1}_{2.4}$ | 10.7 |
| 5.25(25) | $(n, p_0)$ | $61.9 \pm^{5.5}_{9.5}$ | 73.8 |
| 5.25(25) | $(n, p_1)$ | $13.2 \pm^{2.9}_{2.5}$ | 21.1 |
| 5.25(25) | $(n, p_2)$ | $34.8 \pm^{5.4}_{5.5}$ | 46.7 |
| 5.25(25) | $(n, p_3)$ | $17.6 \pm^{3.6}_{3.2}$ | 25.2 |
| 5.25(25) | $(n, p_4)$ | $14.7 \pm^{3.7}_{2.9}$ | 23.0 |
| 5.25(25) | $(n, p_5)$ | $11.7 \pm^{2.1}_{2.3}$ | 14.0 |
| 5.75(25) | $(n, p_0)$ | $46.9 \pm^{3.2}_{7.6}$ | 55.6 |
| 5.75(25) | $(n, p_1)$ | $9.1 \pm^{2.3}_{1.8}$ | 18.4 |
| 5.75(25) | $(n, p_2)$ | $27.8 \pm^{6.1}_{4.7}$ | 41.9 |
| 5.75(25) | $(n, p_3)$ | $16.4 \pm^{4.5}_{3.0}$ | 23.2 |
| 5.75(25) | $(n, p_4)$ | $17.0 \pm^{4.2}_{3.4}$ | 23.0 |
| 5.75(25) | $(n, p_5)$ | $12.0 \pm^{3.4}_{2.4}$ | 14.9 |
| 2.75(25) | $(n, \alpha_{0,1})$ | $5.0 \pm^{3.0}_{1.8}$ | 6.7 |
| 3.25(25) | $(n, \alpha_{0,1})$ | $29.0 \pm^{1.8}_{5.3}$ | 20.1 |
| 3.75(25) | $(n, \alpha_{0,1})$ | $59.1 \pm^{3.7}_{10.7}$ | 46.7 |
| 4.25(25) | $(n, \alpha_{0,1})$ | $79.8 \pm^{4.7}_{14.4}$ | 76.0 |
| 4.75(25) | $(n, \alpha_{0,1})$ | $89.0 \pm^{4.9}_{16.0}$ | 94.0 |
| 5.25(25) | $(n, \alpha_{0,1})$ | $90.0 \pm^{5.5}_{16.3}$ | 98.0 |
| 5.75(25) | $(n, \alpha_{0,1})$ | $87.5 \pm^{6.5}_{15.3}$ | 87.0 |
| 5.75(25) | $(n, \alpha_{3,4})$ | $47 \pm^{2.0}_{7.5}$ | 43.0 |



FIG. 10. $(n, p)$ reaction channels leading to higher excited states in $^{35}S$ are observed at higher incident neutron energies.

section for populating the $^{35}S_{g.s.}$ and is shown in Fig. 12 for three different flight path lengths. In each panel, the results show peaks in the cross section that appear at time-of-flight
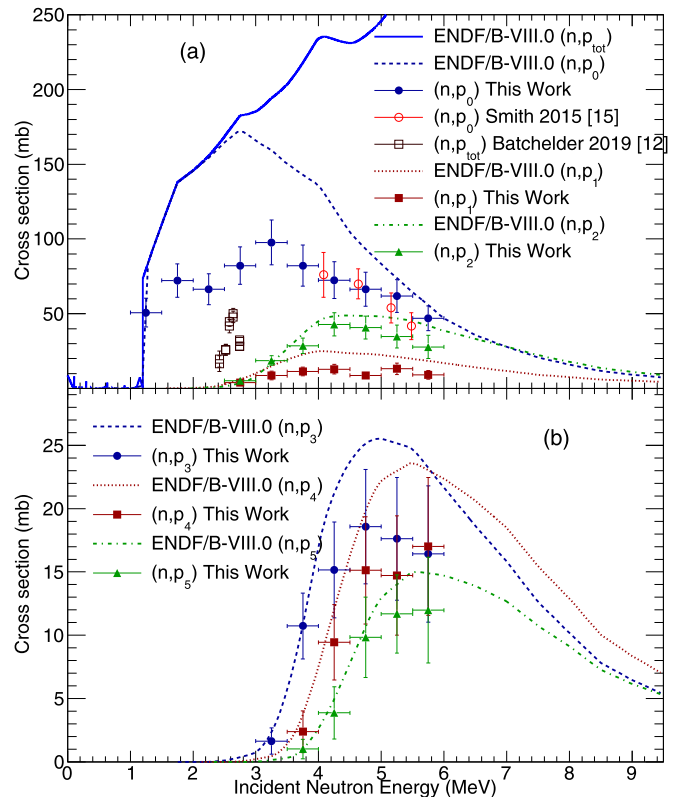


FIG. 11. Partial angle-integrated cross sections in 500 keV wide bins are shown in comparison to the ENDF/B-VIII.0 evaluated partial cross sections for $(n, p)$ reactions up to (a) the first two excited states of $^{35}S$ and (b) up to $(n, p_5)$ The results in this work show a significant reduction relative to the ENDF/B-VIII.0 cross section for the $(n, p_0)$ reaction channel between 1 and 5 MeV and a slight reduction for the excited states.
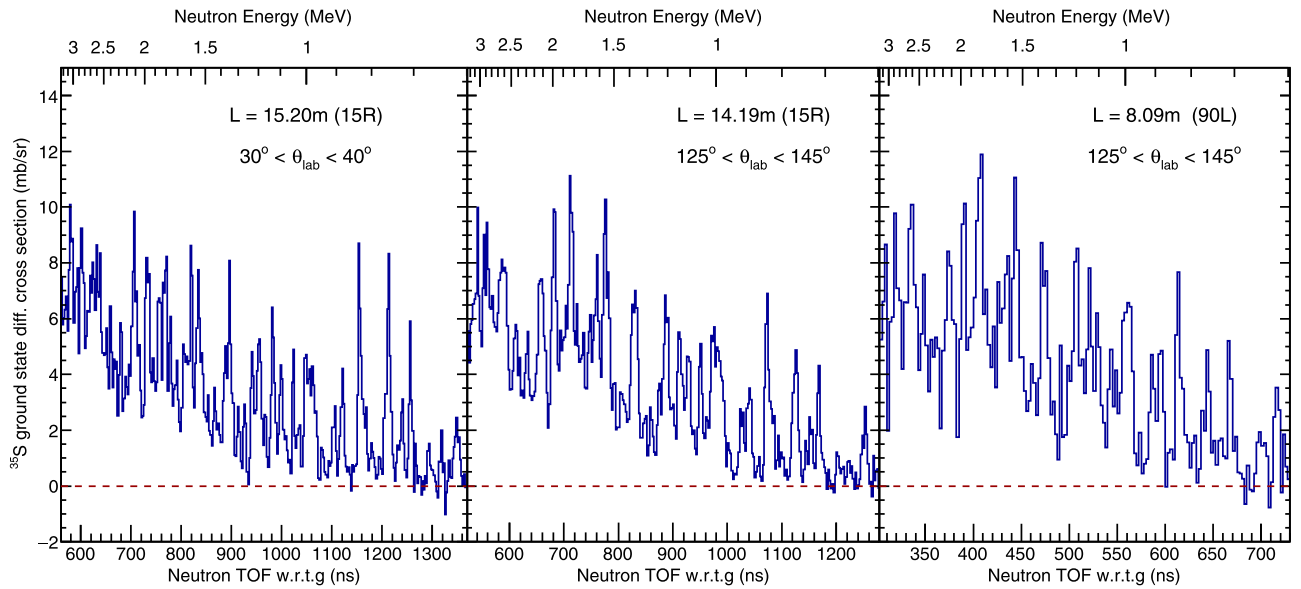
FIG. 12. Differential cross section data for populating the ground state of $^{35}$S for different flight paths, flight path lengths, and laboratory angles. The dominant resonance structures are observed in all cases with consistent energies.

values corresponding to equivalent neutron energies. This provides confidence in the determination of the absolute flight path lengths and that the origin of these peaks are more than just statistical fluctuations.

A second conclusion presented in Ref. [12] is that a resolved resonance approach to calculations of the cross section may be necessary rather than a purely Hauser-Feshbach (HF) treatment up to approximately 3 MeV. Further discussion on applying a HF formalism to reproduce the energy averaged experimental data from this work is presented in Sec. IV, however, the finely binned $^{35}$S$_{g.s.}$ data from this work definitively confirms that a nonstatistical treatment is necessary to precisely treat the $^{35}$Cl($n, p$)$^{35}$S cross section beyond the 1 MeV that was originally considered in the ENDF/B-VIII.0 evaluation.

Among the many peaks that we observe, there is a peak with a centroid at $E_n \approx 2.61(2)$ MeV that is consistent with the structure observed in Ref. [12]. Although the energy is compatible, the absolute value of the cross section data at this energy range is inconsistent, which may suggest some discrepancy with regards to their relative normalization. In their work, this peak was identified as being consistent with a state in $^{36}$Cl that was identified at an excitation energy of 11.24 MeV in a study of the $^{37}$Cl($^3$He, $\alpha$) reaction [35]. From there, they performed an analysis under the assumption that the energy dependence of their measured cross section is dominated by an isolated resonance at this energy. However, based on the data from this work, it seems more likely that the cross section is determined by the combined contributions from multiple resonances.

This is evidenced in the angle-integrated partial cross section for the ground state channel that is shown in Fig. 13(b) and compared with ENDF/B-VIII.0 for the ($n$, total) cross section [Fig. 13(a)] and ($n, p$) cross section [Fig. 13(b)]. Although the energy resolution in this work is not as precise

as the ($n$,total) data, contributions due to analog resonances in the ($n$,total) cross section evaluation appear to be contributing more significantly in the ($n, p$) data than originally predicted in the resonance analysis.

## IV. THEORETICAL CONSIDERATIONS

### A. Neutron entrance channel

In comparison with previous evaluations for $^{35}$Cl in ENDF/B-VIII.0 [1] that employ a statistical HF calculation above 1.2 MeV, the experimental data from this work and Batchelder *et al.* [12] suggest that a significant reduction in the compound nuclear reactions is needed. This also applies to the data below 1.2 MeV when the HF calculation is extrapolated into the resolved resonance region. The proximity for the mass-range understudy to the $N = Z = 20$ shell gap strongly indicates that a statistical calculation with a global set of optical potentials such as Koning-Delaroche [37] may not be appropriate by two major reasons; a nuclear deformation effect and hindrance of neutron absorption due to low level densities near the neutron separation energy in $^{36}$Cl. This can be seen in the upper panel in Fig. 14. The absorption (compound formation) cross sections by the Koning-Delaroche potential are already in the same magnitude as the evaluated total cross section in the 0.1–0.4 MeV range, while the calculated total cross sections are much higher than the evaluated values up to 2 MeV.

The low-lying levels in $^{35}$Cl show a rotational band structure of $(3/2)^+$, $(5/2)^+$, and $(7/2)^+$, and the finite range droplet model (FRDM) [38,39] gives the deformation parameters of $\beta_2 = -0.25$ and $\beta_4 = -0.15$. We perform the coupled-channels calculation for $^{35}$Cl with the Kunieda optical potential [40] for this coupling-scheme, which reduces the absorption cross section in the hundred-keV region, shown in Fig. 14(a), but insufficiently.
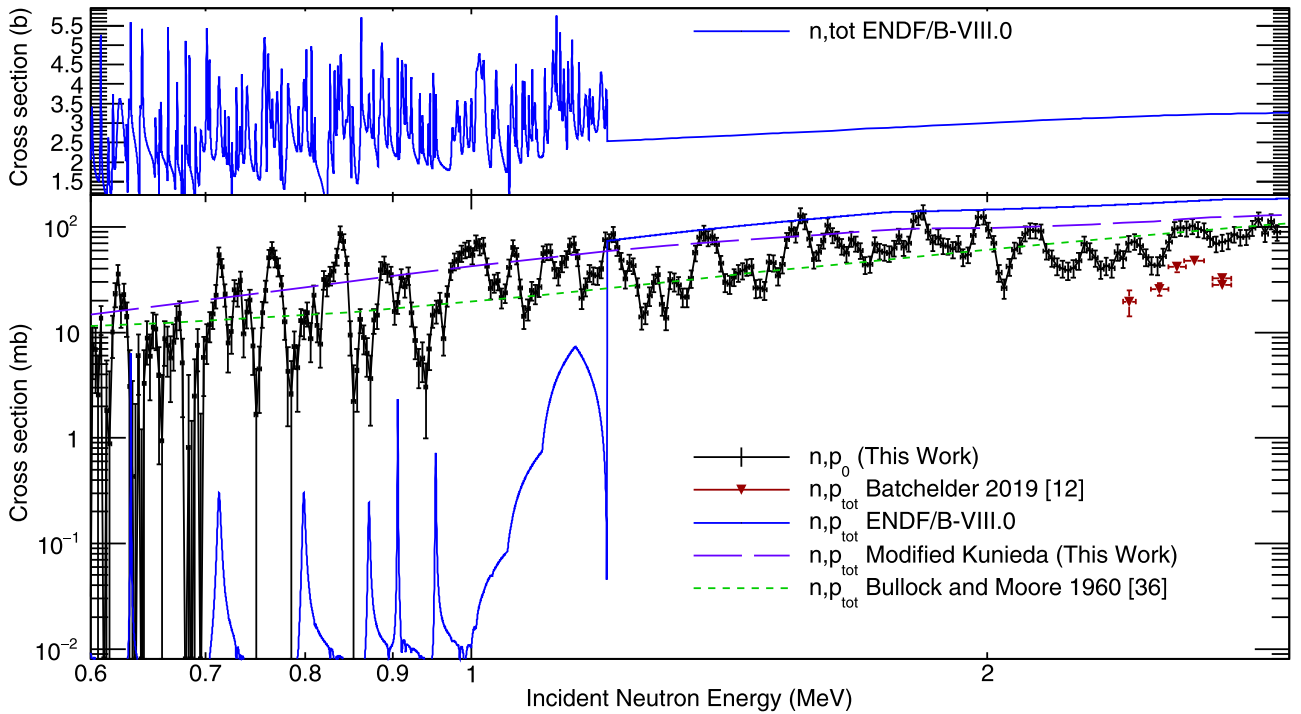
FIG. 13. Bottom: The partial angle-integrated cross section for populating the ground state of $^{35}$S. The data are reasonably well bounded, albeit with significant fluctuations, by the calculated results adopted from Ref. [36], and from the statistical calculation employing a modified Kunieda potential from this work. For comparison, the top panel shows the resonance structures in the $^{35}$Cl($n$,total) spectrum of ENDF/B-VIII.0. The resonances that we observe in the $(n, p)$ data are clearly the sum of multiple narrower resonances that appear to have analogues in the ($n$,total) data but are not strongly represented in the $(n, p)$ evaluation below 1 MeV.

A simple combinatorial calculation of the $^{36}$Cl level density clearly shows that there is significant structure as well as staggering between parities in the excitation range of interest above the neutron separation energy. Such "nonstatistical" properties in a compound nucleus cannot be incorporated into the model calculations, hence we introduce a phenomenological reduction in the absorption cross section by adjusting the Kunieda potential in the low energy region. Since the parameters in the Kunieda potential are energy dependent, the modifications are made by applying scaling factors to the potential parameters, which vary linearly with the neutron incident energy. The scaling factor for the depth of the real potential $V$ is 1.06 at zero energy, and linearly increases to 1.1 at 5 MeV. The real potential diffuseness $a_V$, the surface imaginary potential depth $W$, and the imaginary potential diffuseness $a_W$ have the factors of 0.85, 0.85, and 0.75 at zero energy, and the increase linearly to 5 MeV. Above 5 MeV the potential parameters are the same as those in the Kunieda potential except for the scaling factor of 1.1 applied to $V$. These parameters are derived from not only the evaluated total cross sections but also the s- and p-wave strength functions. This set gives $S_0 = 0.625 \times 10^{-4}$ and $S_1 = 1.17 \times 10^{-4}$, which are comparable to the resonance analysis values of $S_0 = (0.59 \pm 0.12) \times 10^{-4}$ and $S_1 = (1.11 \pm 0.12) \times 10^{-4}$ [5]. The calculated total and absorption cross sections are shown in Fig. 14(b), which reasonably reproduces the evaluated and experimental total cross sections albeit the modifications are rather crude. Since the Kunieda potential is isospin consistent, we ap-

ply the same modification to the proton channel in the HF calculation.

### B. Statistical model calculation

We carry out the HF calculation with the COH3 code [30], where the coupled-channels optical model is integrated in the statistical model. Direct reactions to the strongly coupled inelastic scattering channels are properly included in the HF model by performing the so-called Engelbrecht-Weidenmüller transformation [43–45]. The optical potentials for the neutron and proton channels are the modified Kunieda-potential as derived above. For the $\alpha$-particle and deuteron channels, we employ the global potentials of Avrigeanu *et al.* [46] and Bojowald *et al.* [47]. Because the $^{35}$Cl($n, \gamma$) cross section in the hundred-keV region is typically in the order of mb or less, uncertainties in the photon strength function do not affect much our reaction modeling for the charged particle emission. We took the average photon width $\langle \Gamma_\gamma \rangle$ of 0.561 eV [5].

The calculated partial $^{35}$Cl($n, p$) cross sections are compared with the measured data in Fig. 15. Because the Coulomb barrier suppresses the proton emission that leaves $^{35}$S at higher excited states, the $^{35}$Cl($n, p_0$) channel has the largest cross section in the energy range of our interest. While the cross section for the first excited state $(n, p_1)$ is lower than $(n, p_2)$. This reversal is due to the odd parity of 3.484 MeV level in $^{35}$S. When a 3-MeV neutron interacts with $^{35}$Cl, the proton center-of-mass energy for the $(n, p_2)$ is 1.54 MeV. At
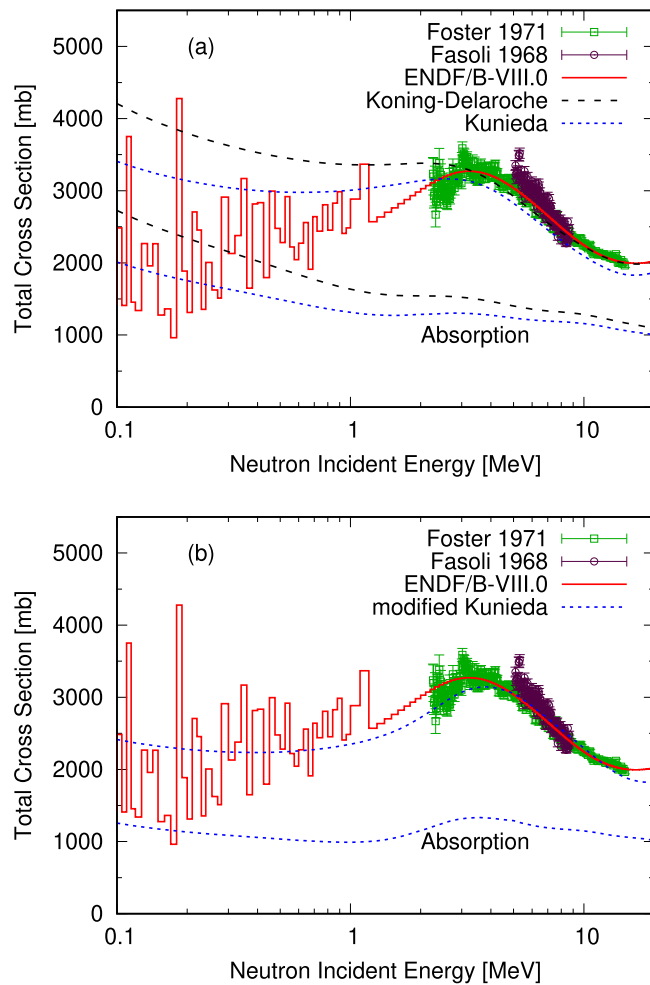
FIG. 14. (a) Calculated total cross sections for $^{35}$Cl with the Koning-Delaroche spherical optical potential and Kunieda coupled-channel potential are compared with the evaluated cross section of ENDF/B-VIII.0 (histogram) and the experimental data of Foster and Glasgow [41] and Fasoli *et al.* [42]. The experimental data are for natural chlorine. (b) Comparisons with modified coupled-channels potential. In the resonance region, the evaluated total cross sections are group-averaged for better visibility.



FIG. 15. Comparisons of calculated and experimental $^{35}$Cl$(n, p_x)$ cross sections, where $x = 0$ and 1 in (a) and $x = 2$, 3, 4, and 5 in (b). The comparison between the calculated and experimental $^{35}$Cl$(n, \alpha_0 + \alpha_1)$ cross section is also shown in (a).

this energy the $p$-wave proton transmission coefficient is the largest, hence the proton emission is enhanced when parity changes. Note that roughly the same number of even and odd states are populated by an incoming neutron at 3 MeV.

Although the calculation for the $(n, p_0)$ reaction overestimates the experimental data, the $(n, p_1)$ and $(n, p_2)$ are in reasonably good agreement with the data. In the statistical HF model calculation, the proton production cross sections for discrete levels tend to behave in a similar way; when we reduce $(n, p_0)$ for better reproduction of the data, discrepancies in the $(n, p_1)$ and $(n, p_2)$ channels grow. In this sense, the statistical HF calculation gives reasonable ratios to the discrete states, while the absolute magnitude depends on the optical potentials employed.

Figure 15(a) shows the $^{35}$Cl$(n, \alpha_0 + \alpha_1)$ reaction cross sections. Due to the limited experimental resolution, the cross sections to the ground and the first excited states in $^{32}$P
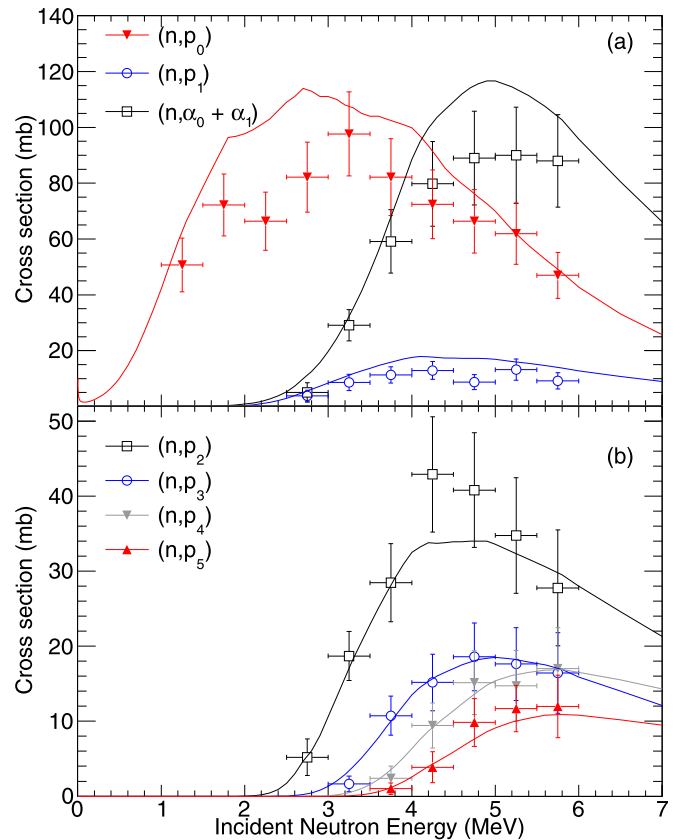
are lumped. The calculation follows the measurements up to 4 MeV, and overshooting above there. This difference might be mitigated by applying a phenomenological adjustment to the $\alpha$-particle optical potential, as done for the neutron channel.

Having reasonable reproduction of the partial $(n, p_x)$ cross sections, we can infer the total $(n, p)$ cross section, which is shown in Fig. 16. The histogram is the reconstructed and group-averaged $(n, p)$ cross section from the resonance parameters in ENDF/B-VIII.0. We also compare the global optical model cases, the spherical optical potential of Koning-Delaroche, and the deformed optical potential of Kunieda *et al.* These two cases give similar $(n, p)$ cross sections despite the compound formation cross sections differ as seen in Fig. 14(a). The modified Kunieda-potential yields always lower $(n, p)$ cross section due to the less-absorption nature. Our modification to the optical potential reduces the $(n, p)$ cross section by 30% at 2 MeV.

In the 100 keV to 1 MeV energy range, there are significant difference between the evaluated and the HF model calculated cross sections. The evaluation reveals an abrupt jump at 1.2 MeV that is the boundary of resolved resonance region. This is in stark contrast to the total cross section, where the cross section behaves continuously, yet the fluctuation still persists. The discontinuous behavior of the evaluated $(n, p)$
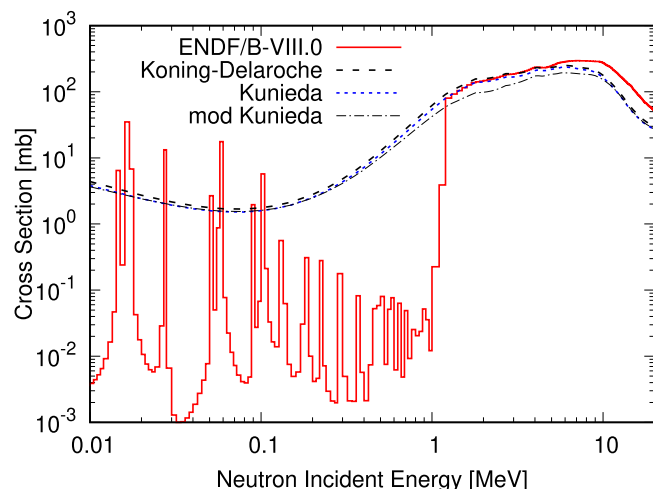
FIG. 16. Calculated total $(n, p)$ cross sections with the Koning-Delaroche spherical optical potential (dashed curve), the Kunieda deformed optical potential (dotted curve), and the modified Kunieda potential (dot-dashed curve), compared with the evaluated cross section given in ENDF/B-VIII.0. The ENDF cross sections below 1.2 MeV are reconstructed from the resolved resonance parameters, and group-averaged.

cross section happens because a limited number of resonances in the hundred-keV region have a sufficiently large proton width. Our statistical treatment of proton emission implicitly assumes that all of the resonances could have the proton channel, and their width has some statistical distributions around the average $\langle \Gamma_p \rangle$. We cannot obtain the actual $\Gamma_p$ for each resonance unless enough high-resolution $(n, p)$ data are available for the $R$-matrix analysis. An approximation, which is often done for the radiative capture channel, is to assume $\Gamma_p$ can be replaced by their average $\langle \Gamma_p \rangle$. The statistical HF calculation gives the average proton widths $\langle \Gamma_p \rangle$ of 0.0492 eV for $J^\pi = 1^+$ and 0.0464 eV for $J^\pi = 2^+$.

## V. SUMMARY

The $^{35}$Cl$(n, p)$$^{35}$S reaction cross section has been studied from 600 keV to 6 MeV using spallation neutrons from the WNR facility at Los Alamos Neutron Science Center. In the most recent ENDF/B-VIII.0 evaluation of the $^{35}$Cl$(n, p)$ cross section, a resonant approach is included up to 1.25 MeV with a discontinuous transition to an energy-averaged statistical approach at energies above 1.25 MeV. The definitive nonstatistical behavior of the cross section measured in this work,

up to around 3 MeV, confirms the speculation of Batchelder *et al.* [12] that a statistical Hauser-Feshbach calculation is not sufficient to precisely describe the reaction at energies above 1 MeV. However, we have shown that the general trend of the energy averaged experimental data can be reasonably reproduced with a statistical model with appropriate adjustments made to the proton optical model parameters. The experimental data and resulting calculations show that ENDF/B-VIII.0 underestimates the $(n, p)$ cross section below 1.25 MeV and overestimates the cross section above 1.25 MeV. As a result, it is recommended that a full re-evaluation needs to be done for this system. To aid in this, additional measurements should be taken that span a larger range of energies and with improved precision to resolve the discrepancies between this work and the work of Batchelder *et al.*

A future set of measurements have been proposed to expand the energy range from as low as 1 eV to approximately 20 MeV to provide consistent results for comparison with previous measurements below 600 keV. These measurements could be performed at the WNR facility (unmoderated tungsten target) and the Lujan Neutron Scattering Center (moderated tungsten target) [48] at LANSCE, with similar experimental setups. To better characterize the background and target systematics, we will employ two forms of the enriched $^{35}$Cl, NaCl, and AgCl on either Au or Pt backings. In addition, the uncertainty in the beam normalization will be improved by utilizing modern flux monitor devices such as SREFT [49]. With these changes, differential cross section measurements with total systematic uncertainties at the 5% level should be achievable.

[1] D. A. Brown *et al.*, Nucl. Data Sheets **148**, 1 (2018).

[2] K. Shibata *et al.*, J. Nucl. Sci. Technol. **48**, 1 (2011).

[3] S. Zabrodskaya *et al.*, Nucl. Constants **1**, 3 (2007).

[4] W. Hauser and H. Feshbach, Phys. Rev. **87**, 366 (1952).

[5] R. O. Sayer, K. H. Guber, L. C. Leal, N. M. Larson, and T. Rauscher, Phys. Rev. C **73**, 044603 (2006).

[6] K. H. Guber, P. E. Koehler, D. Wiarda, J. A. Harvey, T. E. Valentine, R. O. Sayer, L. L. Leal, N. M. Larson, T. S. Bigelow,

C. Ausmus, D. R. Brashear, R. B. Overton, J. A. White, and V. M. Cauley, in *International Conference on Nuclear Data for Science and Technology 2007* (EDP Science, 2007), pp. 403–405.

[7] P. E. Koehler, Phys. Rev. C **44**, 1675 (1991).

[8] S. Druyts, C. Wagemans, and P. Geltenbort, Nucl. Phys. A **573**, 291 (1994).

[9] W. Nagel and A. H. W. Aten, Physica **31**, 1091 (1965).

[10] T. Schantl, thesis, Institut fuer Isotopenforschung und kernphysik, 1970 (unpublished).

[11] D. V. Aleksandrov, L. I. Klochkova, and B. S. Kovrigin, At. Energy **39**, 736 (1975).

[12] J. C. Batchelder *et al.*, Phys. Rev. C **99**, 044612 (2019).

[13] T. Brown *et al.*, Nucl. Instrum. Methods Phys. Res. A **954**, 161123 (2018).

[14] P. Chowdhury (private communication).

[15] M. B. Smith *et al.*, Nucl. Instrum. Methods Phys. Res. A **784**, 162 (2015).

[16] N. D'Olympia *et al.*, Nucl. Instrum. Methods Phys. Res. A **763**, 433 (2014).

[17] L. E. Kirsch, M. Devlin, S. M. Mosby, and J. A. Gomez, Nucl. Instrum. Methods Phys. Res. A **874**, 57 (2017).

[18] P. W. Lisowski, C. D. Bowman, G. J. Russell, and S. A. Wender, Nucl. Sci. Eng. **106**, 208 (1990).

[19] H. Y. Lee *et al.* (unpublished).

[20] S. A. Wender *et al.*, Nucl. Instrum. Methods Phys. Res. A **336**, 226 (1993).

[21] www.cividec.at.

[22] http://www.micronsemiconductor.co.uk/.

[23] C. J. Werner (Ed.), "MCNP users manual - code, version 6.2", (2017), https://mcnp.lanl.gov/mcnp_manual.shtml.

[24] F. Tovesson, A. Laptev, and T. S. Hill, Nucl. Sci. Eng. **178**, 57 (2014).

[25] J. F. Ziegler, M. D. Ziegler, and J. P. Biersack, Nucl. Instrum. Methods Phys. Res. B **268**, 1818 (2010).

[26] S. Agostinelli *et al.*, Nucl. Instrum. Methods Phys. Res. A **506**, 250 (2003).

[27] P. Tsintari *et al.* (unpublished).

[28] H. I. Kim *et al.*, Nucl. Instrum. Methods Phys. Res. A **964**, 163699 (2020).

[29] K. Takamiya *et al.*, Appl. Radiat. Isot. **66**, 1321 (2008).

[30] T. Kawano, COH3: the coupled-channels and Hauser-Feshbach code.

[31] H. Adler, P. Huber, and W. Hälg, Helv. Phys. Acta **26**, 349 (1953).

[32] C. Ouellet, B. Singh, Nucl. Data Sheets **112**, 2199 (2011).

[33] J. M. Blatt and L. C. Biedenharn, Rev. Mod. Phys. **24**, 258 (1952).

[34] J. Chen, J. Cameron, and B. Singh, Nucl. Data Sheets **112**, 2715 (2011).

[35] L. Broman, C. M. Fou, and B. Rosner, Nucl. Phys. A **112**, 195 (1968).

[36] R. E. Bullock and R. G. Moore, Phys. Rev. **119**, 721 (1960).

[37] A. J. Koning and J. P. Delaroche, Nucl. Phys. A **713**, 231 (2003).

[38] P. Möller *et al.*, At. Data Nucl. Data Tables **59**, 185 (1995).

[39] P. Möller *et al.*, At. Data Nucl. Data Tables **109–110**, 1 (2016).

[40] S. Kunieda *et al.*, J. Nucl. Sci. Technol. **44**, 838 (2007).

[41] D. Graham Foster, Jr., and D. W. Glasgow, Phys. Rev. C **3**, 576 (1971).

[42] U. Fasoli, P. P. Sambo, D. Toniolo, and G. Zago, EANDC(E)-89, 1968, http://www-nds.iaea.org/EXFOR/20504.003.

[43] C. A. Engelbrecht and H. A. Weidenmüller, Phys. Rev. C. **8**, 859 (1973).

[44] T. Kawano, P. Talou, and H. A. Weidenmüller, Phys. Rev. C **92**, 044617 (2015).

[45] T. Kawano, R. Capote, S. Hilaire, and P. Chau Huu-Tai, Phys. Rev. C **94**, 014612 (2016).

[46] M. Avrigeanu *et al.*, At. Data Nucl. Data Tables **95**, 501 (2009).

[47] J. Bojowald, H. Machner, H. Nann, W. Oelert, M. Rogge, and P. Turek, Phys. Rev. C. **38**, 1153 (1988).

[48] M. Mocko and G. Muhrer, Nucl. Instrum. Methods Phys. Res. A **704**, 27 (2013).

[49] K. T. Schmitt, Spatially resolved fission tag (SREFT) - a low-mass TPC, Technical Report No. LA-UR-18-24582, Los Alamos National Laboratory (LANL), Los Alamos, NM, USA, 2018.